A fracture mechanics analysis of the micromechanical events in finite thickness fibre push-out tests

Benjamin Collard [a,b,*], Finn Giuliani [a], Gerwin Ingenbleek [c], Guy Verbist [c], Daniele Dini [b]

[a] Department of Materials Science, Imperial College London, South Kensington Campus, London, SW7 2AZ, United Kingdom
[b] Department of Mechanical Engineering, Imperial College London, South Kensington Campus, London, SW7 2AZ, United Kingdom
[c] Department of Materials & Construction, Shell Technology Centre Amsterdam, Amsterdam, The Netherlands

ARTICLE INFO

ABSTRACT

Understanding the micromechanical events of interfacial failure in fibre reinforced composites is vital to accurately characterising micromechanical properties and, consequently, the macroscopic properties of the composite. A fracture mechanics model of the fibre push-out test is developed, with an emphasis on the effect of sample thickness and residual stresses on the mechanisms of interfacial crack advancement. The model is applied to both a SiC_f-SiC ceramic matrix composite and a SiC_f-Ti metal matrix composite. The model demonstrates that previous assumptions about the micromechanical events of interfacial cracking are consistent with the measured values of interfacial fracture energy for ceramic matrix composites. Moreover, the model can identify the range of geometries for which different micromechanical cracking mechanisms occur simultaneously in a given material system. Identifying this range is important in choosing the sample geometry for fibre push-out testing because the interaction of advancing cracks affects the measurement of interfacial fracture energy by classical models.

1. Introduction

Fibre reinforced composites are candidate materials across a wide range of applications. The variety of available fibre and matrix materials allow these materials to be tailored for their intended usage. For instance, ceramic matrix composites (CMCs) have excellent stiffness, specific strength and thermal properties. The reinforcing fibres act to prevent the brittle failures associated with monolithic ceramics [1,2]. These properties make CMCs ideal for applications in gas turbines and other high temperature environments [3,4]. Another set of examples are polymer matrix composites (PMCs). These materials are lightweight, flexible and have excellent specific strength. PMCs are employed in a wide range of aerospace applications.

The interface between the fibres and matrix plays a complex role in determining the failure of fibre reinforced composites. Interfacial properties have a strong impact on translaminar fracture toughness in PMCs [5]. In the case of CMCs, interfacial fracture is preferred to fibre fracture. Interfacial failure enables toughening mechanisms for the overall composite such as fibre bridging by crack deflection [2,6]. The interface between fibres and matrix in CMCs is therefore tailored to be weaker. This is frequently accomplished by adding a thin layer of hexagonal boron nitride (BN) [7] or a layer of pyrolytic carbon [8]. Boron nitride is the preferred material for applications such as gas

engine turbines due to its resistance to oxidation. Conversely, PMCs with weak interfaces perform poorly when the polymer matrix undergoes ductile failure. In particular, theoretical and experimental analysis indicates that kink band formation occurs concurrently with interfacial fracture [9]. Interfacial design remains challenging for PMCs.

One popular technique to measure the fracture energy of the interface is the single fibre push-out test [10]. A sample of the material is prepared such that an indenter can apply a displacement to the cross-section of the fibre. The indenter increments the displacement of the fibre, measuring the required load, until the fibre is pushed out of the base of the sample. Recently, authors have adapted the test to be performed in-situ, allowing analysis of the micromechanical events involved in debonding [11]. Efforts to reduce the scatter in data for PMC fibre push-out tests through digital technology have been studied [12].

A range of models exist for the fibre push-out test in ceramic matrix composites. Early models related the interfacial energy to only the increment in strain energy [13]. Authors have since incorporated the effect of the work done by the loading system and the work done in interfacial sliding [14,15]. These models typically use an approach based on shear lag, assuming the push-out sample to have infinite thickness. Accordingly, these models perform well when the sample

---

Nomenclature

Symbols

H	Sample thickness
R_f	Fibre radius
F	Applied load
h	Interfacial coating thickness
R_0	Numerical outer radius
σ	Applied stress
σ_{res}	Residual axial stress
u_f	Axial fibre displacement
σ_f	Axial fibre stress
E_f	Fibre Young modulus
τ	Elastic shear stress
u_m	Matrix displacement in axial direction
G_m	Matrix shear modulus
G_c	Interfacial layer shear modulus
η	Dimensionless exponential parameter
ψ	Dimensionless thickness ratio
$\bar{\tau}$	Interfacial frictional stress
a_t	Crack length at sample top
a_b	Crack length at sample bottom
$G_{\text{II}}(G_{\text{II}}^c)$	(Critical) mode-II energy release rate
δ	Fibre displacement at loading surface
w_s	Permanent sliding displacement
$\alpha,\ \beta,\ \omega$	Quadratic criterion coefficients
κ	Dimensionless residual axial stress balance
γ	Dimensionless interfacial frictional balance
ϕ	Dimensionless critical applied stress ratio for top and bottom debonding

thickness is large and the matrix sufficiently stiff that its compliance can be neglected. One example of such a material system are SiC–SiC composites such as those studied in [16]. A variety of additional effects have been considered, one example being fibre surface roughness [17]. One key finding is that the interfacial friction on debonded fibre lengths has a strong influence on the push-out behaviour and fracture toughness measurement. Recently, authors have considered the influence of an elastic–plastic interfacial layer in a sample of infinite thickness [18]. Semi-analytic techniques are employed more generally throughout the composites literature [19].

Modelling the fibre push-out test for metal matrix composites presents further specific challenges. In particular, the interfacial crack generally propagates from the bottom of the sample during the fibre push-out test [20,21]. It is clearly not valid to apply an assumption of infinite sample thickness in this case, leading to the formulation of range of models [22,23]. Similarly to the model of the push-out test for CMCs, models for MMCs have incorporated interfacial friction, the effect of the loading system and the effect of Poisson expansion near the loading face. These models typically apply a shear lag approach with finite thickness. A key result for the present work is the discussion of the effect of residual axial stresses on the debonding behaviour [22]. Like CMCs, MMCs are proposed as a candidate material for turbine applications, with many advantageous mechanical properties [24].

Semi analytical models of the fibre push-out test remain limited in scope due to the specificity of assumptions required in their formulation. For instance, shear lag approaches assume that the matrix undergoes no deformation [13,22], meaning that these models cannot be applied to soft matrix composites such as PMCs. Additionally, the models discussed take the location of crack initiation as an assumption.

The validity of this assumption is frequently questionable and could explain situations in which the chosen model does not perform well. For example, in the work of [22], the model underestimates the interfacial fracture energy of a SCS-6/Timetal 21 s system. One possible reason for this is that the model cannot capture the interaction of crack fronts in the fibre push-out test. Analysing interacting crack fronts remains very challenging [25] and is undesirable in fibre push-out testing.

Another very common approach to modelling the fibre push-out test is the finite element method [20,26]. The finite element approach solves the full system of elastic partial differential equations numerically and is often used as a validation tool for semi-analytical approaches [18,22]. The finite element method has also been applied to assess the micromechanics of debonding. One key conclusion of a finite element study is that the location of the initiation of the debond in fibre push-out is controlled by the mismatch in elastic coefficients between the fibre and the matrix [26]. The main drawbacks of the finite element approach are that the results can be very time consuming to obtain and do not easily generalise beyond the systems studied.

In the present study, we have formulated a generalised model of the fracture energy of the interface in fibre-reinforced composites. The key dimensionless parameters controlling physical aspects of the test are deduced and the effect of changing these parameters is studied. We analyse CMCs and demonstrate that for realistic testing samples and conditions, the interfacial crack initiates and propagates from the top of the sample. We finally examine the case of the MMCs and demonstrate that debonding typically initiates and propagates from the base of the sample.

2. Fracture mechanics model

A schematic of the fibre push-out test is presented in Fig. 1. The thickness of the sample is denoted by H, the radius of the fibre by R_f, the applied force by F and the thickness of the interfacial coating by h. An outer radius R_0 is defined to be much greater than R_f. Given an applied compressive load F on the face $z = H/2$, we must compute the axial stress distribution in the fibre. Additionally, we must consider the effect of residual stresses in the fibre. Let us assume that the residual stresses act in tension on the fibre faces. Let the applied stress of the load F be denoted by $\sigma = F/\pi R_f^2$.

We will modify the analysis of Callaway [18] by introducing an elastic axial residual stress. Such a residual stress arises due to the mismatch between thermoelastic properties of the fibre and the matrix. The sample should retain rotational symmetry, suggesting that the residual stress on the top and bottom faces should be equal in magnitude but opposite in direction. Let the axial residual stress on the top face be denoted by σ_{res}. The axial residual stress on the bottom face is therefore $-\sigma_{\text{res}}$. Note that in general, the direction of the residual stress is specific to the choice of fibre and matrix. We will assume that the residual stress at the top of the fibre acts in the opposite direction to the loading.

Let the sample have finite thickness H. To accommodate the finite thickness of the sample, we must alter the coordinate system such that the sample lies in the interval $[-H/2, H/2]$, reversing the direction of increasing z. In this coordinate system, we express Hooke's law by:

$$\frac{\partial u_f}{\partial z}(z) = \frac{\sigma_f(z)}{E_f}. \tag{1}$$

The shear lag approach to the equations of elasticity is taken. Previous work demonstrates that the shear lag approach is insufficient to describe the state of interfacial stress in general, particularly for sample thicknesses between 2–5 times the fibre radius [20,27]. However, recent work has demonstrated that the shear lag approach can accurately represent a range of material systems and sample geometries
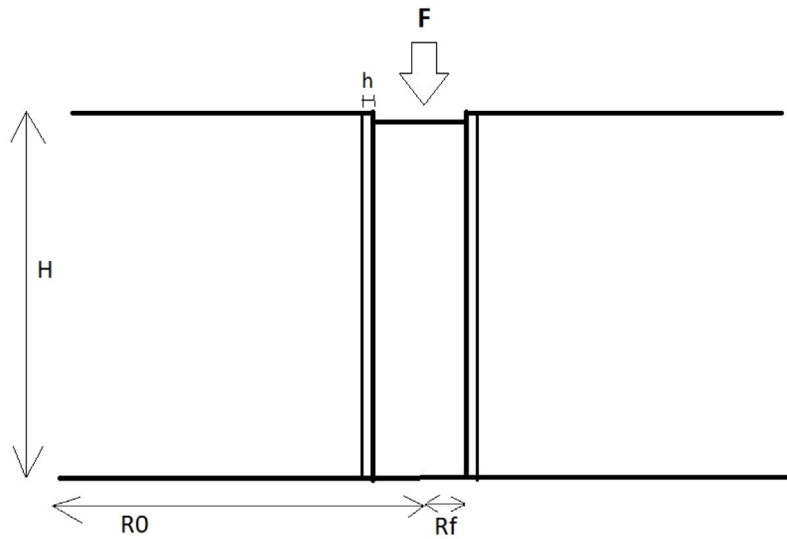
Fig. 1. A figure illustrating the simplified geometry of the fibre push-out test applied in the formulation of the shear lag model.

when appropriately modified [16,18,22]. This further demonstrates the care that must be taken when selecting a model appropriate for the sample geometry and material system in fibre push-out. The equation of shear lag is:

$$\frac{\partial \sigma_f}{\partial z}(z) = \frac{2\tau(z)}{R_f}. \tag{2}$$

The equation of elasticity for the matrix is given by:

$$\frac{\partial u_m}{\partial r}(z) = \frac{R_f \tau(z)}{r G_m}. \tag{3}$$

Integrating Eq. (3), the displacement of the coating at the boundary with the matrix is:

$$u_m(z) = \int_{R_f + h}^{R_0} \frac{R_f \tau(z)}{r G_m} \, dr$$
$$= \frac{R_f \tau(z)}{G_m} \log\left(\frac{R_0}{R_f + h}\right). \tag{4}$$

The change in displacement across the interface is given by:

$$u_f(z) - u_m(z) = \frac{\tau(z) h}{G_c}. \tag{5}$$

Rearranging for u_f and applying Eq. (2):

$$u_f = \frac{R_f}{2}\left(\frac{h}{G_c} + \frac{R_f}{G_m}\log\left(\frac{R_0}{R_f + h}\right)\right)\frac{\partial \sigma_f}{\partial z}(z). \tag{6}$$

Finally, combining with Eq. (1), the governing equation is:

$$\sigma_f(z) - \frac{E_f R_f}{2}\left(\frac{h}{G_c} + \frac{R_f}{G_m}\log\left(\frac{R_0}{R_f + h}\right)\right)\frac{\partial^2 \sigma_f}{\partial z^2}(z) = 0. \tag{7}$$

A dimensionless parameter appears in this governing equation. Let η be defined by:

$$\eta^2 = \frac{E_f}{2}\left(\frac{h}{R_f G_c} + \frac{1}{G_m}\log\left(\frac{R_0}{R_f + h}\right)\right). \tag{8}$$

Demanding that $\sigma_f(H/2) = \sigma + \sigma_{res}$ and that $\sigma_f(-H/2) = -\sigma_{res}$, the solution to Eq. (7) is:

$$\sigma_f(z) = \frac{\sigma}{2\cosh\left(\frac{H}{2\eta R_f}\right)}\cosh\left(\frac{z}{\eta R_f}\right) + \frac{\sigma + 2\sigma_{res}}{2\sinh\left(\frac{H}{2\eta R_f}\right)}\sinh\left(\frac{z}{\eta R_f}\right). \tag{9}$$

Another dimensionless parameter has been deduced. Let us denote $\psi = H/2\eta R_f$. Applying Eq. (2), we obtain the shear stress distribution:

$$\tau(z) = \frac{1}{2\eta}\left(\frac{\sigma}{2\cosh(\psi)}\sinh\left(\frac{z}{\eta R_f}\right) + \frac{\sigma + 2\sigma_{res}}{2\sinh(\psi)}\cosh\left(\frac{z}{\eta R_f}\right)\right). \tag{10}$$

Examples of the axial and shear stress fields in the fibre for different applied axial stresses σ are given in Fig. 2. The material parameters are given by the information for a SiC/SiC composite in Table 2.

Let us suppose that we have non-interacting cracks from the top face and the bottom face of length a_t and a_b respectively. When the bottom crack advances, the residual and applied stresses are relaxed. On the crack faces, axial stress is induced only by constant frictional resistance to sliding, the sliding stress $\bar{\tau}$. We therefore solve Eq. (2) with $\tau(z) = \bar{\tau}$, subject to $\sigma_f(-H/2) = 0$:

$$\sigma_f(z) = \frac{2\bar{\tau}}{R_f}\left(z + \frac{H}{2}\right), \quad z \in \left[-\frac{H}{2}, a_b - \frac{H}{2}\right). \tag{11}$$

When the top crack advances, the fibre remains constrained and cannot deform to relax the applied stress or the residual stresses. Assuming that the sliding stress is equal to the same sliding stress as in crack advancement from the bottom, the axial stress in this debonded region is:

$$\sigma_f(z) = \frac{2\bar{\tau}}{R_f}\left(z - \frac{H}{2}\right) + \sigma + \sigma_{res}, \quad z \in \left(\frac{H}{2} - a_t, \frac{H}{2}\right]. \tag{12}$$

Note that in general, the sliding stress is greater at the top of the fibre than the bottom. The Poisson effect causes the fibre to expand at the top of the sample, inducing radial compressive stresses at the interface. Moreover, in thin samples, the bending response of the material causes radial compression at the top and tension at the base. Considering the Coulomb type law $\bar{\tau} = \tau_0 - \mu\sigma_{rr}$, $\bar{\tau}$ is generally greater in absolute value on the top crack face. This promotes crack advancement from the bottom of the sample.

We will consider three contributions to the energy of the system and deduce formulae for the mode II energy release rate when a crack advances from the top and from the bottom. Let E_{end} denote the work done in the end-shortening of the fibre, E_{elast} denote the elastic energy stored in the system and E_{fric} denote the work done in frictional sliding.
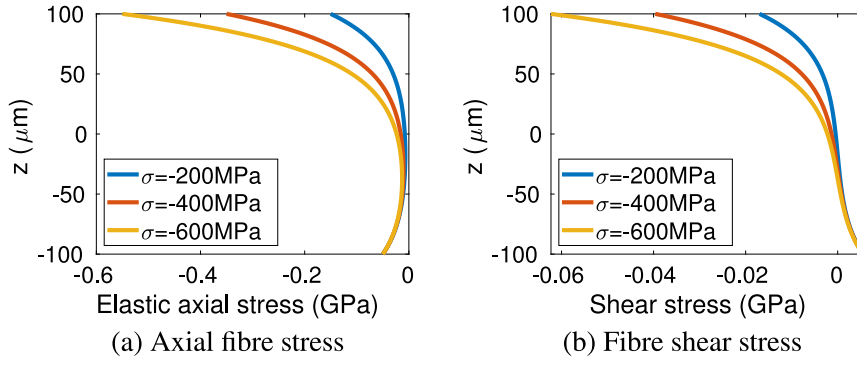
(a) Axial fibre stress

(b) Fibre shear stress

Fig. 2. Figures demonstrating how the elastic stresses vary through the thickness of a sample 200 μm thick with different applied axial stresses σ. The material parameters for this example are given in Table 2.

The energy release rate, defined in terms of the work done per unit area in crack advancement, is given by:

$$G_{\text{II}} = \frac{dE_{\text{end}}}{dA} + \frac{dE_{\text{elast}}}{dA} + \frac{dE_{\text{fric}}}{dA}. \tag{13}$$

Note that for a crack of length a, the crack area is $2\pi R_f a$, implying that:

$$\frac{d}{dA} = \frac{1}{2\pi R_f} \frac{d}{da} \tag{14}$$

The end-shortening distance δ is defined by:

$$\begin{aligned}
\delta &= \int_{-H/2}^{H/2} \frac{\sigma_f(z)}{E_f} \, dz \\
&= \frac{1}{E_f} \left(\int_{-H/2}^{a_b - H/2} \frac{2\bar{\tau}}{R_f} \left(z + \frac{H}{2} \right) \, dz \right. \\
&\quad + \int_{a_b - H/2}^{H/2 - a_t} \frac{\sigma}{2\cosh(\psi)} \cosh\left(\frac{z}{\eta R_f} \right) + \frac{\sigma + 2\sigma_{\text{res}}}{2\sinh(\psi)} \sinh\left(\frac{z}{\eta R_f} \right) \, dz \\
&\quad + \left. \int_{H/2 - a_t}^{H/2} \frac{2\bar{\tau}}{R_f} \left(z - \frac{H}{2} \right) + \sigma + \sigma_{\text{res}} \, dz \right)
\end{aligned} \tag{15}$$

The work done in end-shortening the fibre is given by:

$$E_{\text{end}} = F\delta = \pi R_f^2 \sigma \delta. \tag{16}$$

It can be shown (see Appendix A) that the energy release rate associated to end shortening when the crack propagates from the top of the sample is:

$$\frac{dE_{\text{end}}}{dA_t} = \frac{\sigma R_f}{2E_f} \left(\sigma + \sigma_{\text{res}} - \frac{2\bar{\tau}}{R_f} a_t - \frac{\sigma \cosh\left(\psi - \frac{a_t}{\eta R_f} \right)}{2\cosh(\psi)} \right.$$

$$\left. - \frac{(\sigma + 2\sigma_{\text{res}}) \sinh\left(\psi - \frac{a_t}{\eta R_f} \right)}{2\sinh(\psi)} \right). \tag{17}$$

The energy release rate associated to end shortening when the crack develops from the bottom of the sample is:

$$\frac{dE_{\text{end}}}{dA_b} = \frac{\sigma R_f}{2E_f} \left(\frac{2\bar{\tau}}{R_f} a_b - \frac{\sigma \cosh\left(\frac{a_b}{\eta R_f} - \psi \right)}{2\cosh(\psi)} \right.$$

$$\left. - \frac{(\sigma + 2\sigma_{\text{res}}) \sinh\left(\frac{a_b}{\eta R_f} - \psi \right)}{2\sinh(\psi)} \right). \tag{18}$$

Consider now the elastic energy stored in the system. There are two non-trivial stress components, σ_f and τ, acting on the fibre. The shear stress additionally deforms the layer of interface material when such a layer is present. We therefore have three elastic energies stored within the system:

$$E_{\text{elast},\sigma}^f = \pi R_f^2 \int_{-H/2}^{H/2} \frac{\sigma_f(z)^2}{2E_f} \, dz$$

$$E_{\text{elast},\tau}^f = \pi R_f^2 \int_{-H/2}^{H/2} \frac{\tau(z)^2}{2G_f} \, dz \tag{19}$$

$$E_{\text{elast},\tau}^i = \pi((R_f + h)^2 - R_f^2) \int_{-H/2}^{H/2} \frac{\tau(z)^2}{2G_c} \, dz.$$

In Appendix A, it is demonstrated that the energy release rates in top debonding associated to these stored energies are:

$$\frac{dE_{\text{elast},\sigma}^f}{dA_t} = \frac{R_f}{4E_f} \left(\left(\sigma + \sigma_{\text{res}} - \frac{2\bar{\tau}}{R_f} a_t \right)^2 - \left(\frac{\sigma \cosh\left(\psi - \frac{a_t}{\eta R_f} \right)}{2\cosh(\psi)} \right.\right.$$

$$\left.\left. + \frac{(\sigma + 2\sigma_{\text{res}}) \sinh\left(\psi - \frac{a_t}{\eta R_f} \right)}{2\sinh(\psi)} \right)^2 \right)$$

$$\frac{dE_{\text{elast},\tau}^f}{dA_t} = \frac{R_f}{4G_f} \left(\bar{\tau}^2 - \frac{1}{4\eta^2} \left(\frac{\sigma \sinh\left(\psi - \frac{a_t}{\eta R_f} \right)}{2\cosh(\psi)} \right.\right.$$

$$\left.\left. + \frac{(\sigma + 2\sigma_{\text{res}}) \cosh\left(\psi - \frac{a_t}{\eta R_f} \right)}{2\sinh(\psi)} \right)^2 \right) \tag{20}$$

$$\frac{dE_{\text{elast},\tau}^i}{dA_t} = \frac{\left((h + R_f)^2 - R_f^2 \right)}{4R_f G_c} \left(\bar{\tau}^2 - \frac{1}{4\eta^2} \left(\frac{\sigma \sinh\left(\psi - \frac{a_t}{\eta R_f} \right)}{2\cosh(\psi)} \right.\right.$$

$$\left.\left. + \frac{(\sigma + 2\sigma_{\text{res}}) \cosh\left(\psi - \frac{a_t}{\eta R_f} \right)}{2\sinh(\psi)} \right)^2 \right).$$

The energy release rates in bottom debonding are given by:

$$\frac{d E_{\mathrm{elast},\sigma}^{f}}{d A_b} = \frac{R_f}{4 E_f}\left(\left(\frac{2\bar{\tau}}{R_f}a_b\right)^2 - \left(\frac{\sigma \cosh\left(\frac{a_b}{\eta R_f} - \psi\right)}{2\cosh(\psi)}\right.\right.$$
$$\left.\left. + \frac{(\sigma + 2\sigma_{\mathrm{res}})\sinh\left(\frac{a_b}{\eta R_f} - \psi\right)}{2\sinh(\psi)}\right)^2\right)$$

$$\frac{d E_{\mathrm{elast},\tau}^{f}}{d A_b} = \frac{R_f}{4 G_f}\left(\bar{\tau}^2 - \frac{1}{4\eta^2}\left(\frac{\sigma \sinh\left(\frac{a_b}{\eta R_f} - \psi\right)}{2\cosh(\psi)}\right.\right.$$

$$\left.\left. + \frac{(\sigma + 2\sigma_{\mathrm{res}})\cosh\left(\frac{a_b}{\eta R_f} - \psi\right)}{2\sinh(\psi)}\right)^2\right)$$ (21)

$$\frac{d E_{\mathrm{elast},\tau}^{i}}{d A_b} = \frac{\left((h + R_f)^2 - R_f^2\right)}{4 R_f G_c}\left(\bar{\tau}^2 - \frac{1}{4\eta^2}\left(\frac{\sigma \sinh\left(\frac{a_b}{\eta R_f} - \psi\right)}{2\cosh(\psi)}\right.\right.$$

$$\left.\left. + \frac{(\sigma + 2\sigma_{\mathrm{res}})\cosh\left(\frac{a_b}{\eta R_f} - \psi\right)}{2\sinh(\psi)}\right)^2\right).$$

The final contribution to the energy of the system is that made by the work done against friction. In order to compute this contribution, we must determine the inelastic sliding distance. Observe that the axial displacement of the fibre is continuous. Continuity implies that the sliding distance is the difference between the displacement induced by the axial friction force and the displacement induced by the elastic field. Denoting the sliding displacement at a point z by $w_s(z)$, in the region of the top crack, we must have:

$$w_s(z) = \frac{1}{E_f}\left| \int_{H/2-a_t}^{z} \frac{\sigma \cosh\left(\frac{\bar{z}}{\eta R_f}\right)}{2\cosh(\psi)} + \frac{(\sigma + 2\sigma_{\mathrm{res}})\sinh\left(\frac{\bar{z}}{\eta R_f}\right)}{2\sinh(\psi)} \right.$$

$$\left. - \frac{2\bar{\tau}}{R_f}\left(\bar{z} - \frac{H}{2}\right) - \sigma - \sigma_{\mathrm{res}}\, d\bar{z}\right|.$$ (22)

The sliding distance for the case of crack advancement from the bottom of the sample is:

$$w_s(z) = \frac{1}{E_f}\left| \int_{z}^{a_b - H/2} \frac{\sigma \cosh\left(\frac{\bar{z}}{\eta R_f}\right)}{2\cosh(\psi)} + \frac{(\sigma + 2\sigma_{\mathrm{res}})\sinh\left(\frac{\bar{z}}{\eta R_f}\right)}{2\sinh(\psi)} \right.$$

$$\left. - \frac{2\bar{\tau}}{R_f}\left(\bar{z} + \frac{H}{2}\right)\, d\bar{z}\right|.$$ (23)

The expressions for the total work done against friction are:

$$E_{\mathrm{fric},t} = 2\pi R_f \int_{H/2-a_t}^{H/2} |\bar{\tau}| w_s(z)\, dz$$

$$E_{\mathrm{fric},b} = 2\pi R_f \int_{-H/2}^{a_b - H/2} |\bar{\tau}| w_s(z)\, dz.$$ (24)

It is demonstrated in Appendix A that the expressions for the energy release rate associated to the work done against friction are:

$$\frac{d E_{\mathrm{fric}}}{d A_t} = \frac{|\bar{\tau}| a_t}{E_f}\left(\frac{\sigma \cosh\left(\psi - \frac{a_t}{\eta R_f}\right)}{2\cosh(\psi)} + \frac{(\sigma + 2\sigma_{\mathrm{res}})\sinh\left(\psi - \frac{a_t}{\eta R_f}\right)}{2\sinh(\psi)}\right.$$

$$\left. + \frac{2\bar{\tau} a_t}{R_f} - (\sigma + \sigma_{\mathrm{res}})\right)$$

$$\frac{d E_{\mathrm{fric}}}{d A_b} = \frac{|\bar{\tau}| a_b}{E_f}\left(\frac{\sigma \cosh\left(\frac{a_b}{\eta R_f} - \psi\right)}{2\cosh(\psi)} + \frac{(\sigma + 2\sigma_{\mathrm{res}})\sinh\left(\frac{a_b}{\eta R_f} - \psi\right)}{2\sinh(\psi)}\right.$$

$$\left. - \frac{2\bar{\tau} a_b}{R_f}\right).$$ (25)

We finally formulate the critical energy release rate for the cases of crack advancement from both the top and the bottom of the sample. Observe that the energy release rate associated to crack advancement from the top does not depend on the length of the crack at the bottom of the sample and vice versa. Furthermore, the choice of coordinate system means that the sign of the interfacial fracture energy values differ. Denoting the critical applied stresses for both cases of debonding by σ_c^t and σ_c^b, we have:

$$G_{\mathrm{II}}^c\left(a_t, \sigma_t^a\right) = \frac{d E_{\mathrm{end}}}{d A_t} + \frac{d E_{\mathrm{elast},\sigma}^f}{d A_t} + \frac{d E_{\mathrm{elast},\tau}^f}{d A_t} + \frac{d E_{\mathrm{elast},\tau}^i}{d A_t} + \frac{d E_{\mathrm{fric}}}{d A_t}$$

$$G_{\mathrm{II}}^c\left(a_b, \sigma_b^a\right) = -\left(\frac{d E_{\mathrm{end}}}{d A_b} + \frac{d E_{\mathrm{elast},\sigma}^f}{d A_b} + \frac{d E_{\mathrm{elast},\tau}^f}{d A_b} + \frac{d E_{\mathrm{elast},\tau}^i}{d A_b} + \frac{d E_{\mathrm{fric}}}{d A_b}\right).$$ (26)

One application of the model is to compute the interfacial fracture energy of a test sample. The most challenging parameters to obtain are the sliding stress $\bar{\tau}$ and the elastic residual axial stress σ_{res}. However, by matching the widths of hysteresis loops, $\bar{\tau}$ can be computed [18]. The finite element method is often used to characterise the typical residual stresses in the composite before testing [28]. Given these parameters, we can estimate the interfacial fracture energy in top and bottom crack advancement by fitting the parameter to forward loading data [16].

In order to deduce the actual fracture energy of the interface, we must finally determine which of the computed values is physically relevant. If the values of critical applied stress increase in absolute value with increasing fracture energy, and if the value were the smaller of the two, both cracks would advance. However, our model assumes that only one crack advances, thus proving by contradiction that the relevant value of fracture energy is the larger of the two. Although the assumption is not true in complete generality, we demonstrate that it is true for the material systems studied in the present work. Observe that both energy release rates can be written in the form $\alpha(a)\sigma^2 + \beta(a)\sigma + \omega(a)$. It is sufficient to demonstrate that $\alpha_t(a_t) > 0$ and that $\alpha_b(a_b) > 0$ for all values of crack length. These inequalities are demonstrated to hold in Fig. 3.

It can be shown that the coefficient α depends only on the elastic parameters of the system and the sample geometry. This implies that, regardless of the system interfacial properties and residual stresses, an appropriate test geometry can be found such that the model is valid. Given an experimentally computed value of G_{II}^c, we can deduce the critical applied stress as a function of the crack length. Formulae for σ_c^t and σ_c^b in terms of the quadratic parameters are derived in Appendix B. We will now demonstrate how the micromechanical events in push-out testing vary across the parameter space. Validation and experimental relevance will be provided by application to CMC and MMC systems.
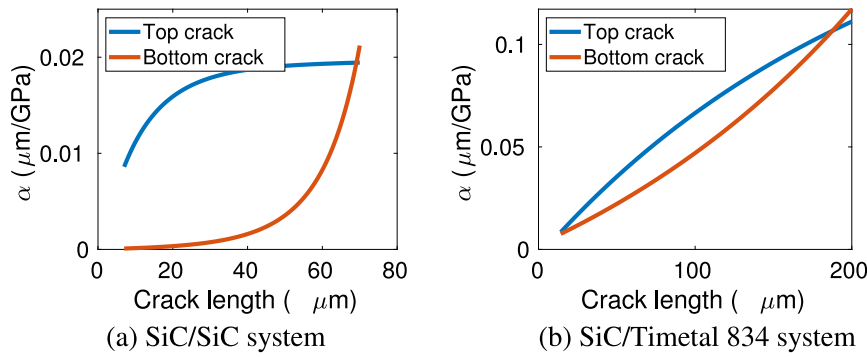
(a) SiC/SiC system   (b) SiC/Timetal 834 system

Fig. 3. Figures demonstrating that the quadratic coefficient α is positive for both material systems considered in this work, for both top and bottom debonding. This implies that the model is valid for these material systems and geometries.

3. Results and discussion

3.1. Dimensional analysis

The key objective in the formulation of the model is the expansion of the fibre push-out test to new material systems. We would like to be able to compute the geometric parameters for which, in a given system, the crack initiated during fibre push-out is stable, not influenced by other crack tips and propagates in a known direction. Since we aim for this analysis to apply in general, we begin with a dimensional analysis of the problem.

In this problem, we aim to determine how the critical applied stress changes with the crack length in dimensionless form. The crack advances on the scale of the shortest length in the sample geometry, typically the fibre radius, suggesting that R_f is a suitable choice for the scale of the crack length. Let us denote the dimensionless crack lengths by $\hat{a}_t$ and $\hat{a}_b$. We expect that the cracking process will be driven by the applied stress overcoming the critical energy release rate Γ. An appropriate scale for the stress is therefore Γ/R_f, denoting the dimensionless applied stress by $\hat{\sigma}$. Analogously, let us denote the dimensionless critical applied stresses by $\hat{\sigma}_t^c$ and $\hat{\sigma}_b^c$.

A number of dimensionless parameters have already been identified in our analysis. The parameter η was identified by Callaway [18], and we have identified the parameter ψ earlier in our analysis. Applying the scales above, we obtain five further parameters:

$$E_f^* = \frac{R_f E_f}{\Gamma}, \quad G_f^* = \frac{R_f G_f}{\Gamma},$$

$$G_c^* = \frac{R_f^3 G_c}{((h + R_f)^2 - R_f^2)\Gamma}, \quad \kappa = \frac{R_f \sigma_{\text{res}}}{\Gamma}, \quad \gamma = \frac{R_f \bar{\tau}}{\Gamma} \quad (27)$$

Note that E_f^*, G_f^* and G_c^* are analogous to the elastic constants in the original problem and are typically large parameters. The parameters ψ and η are grouped together as geometric parameters, while κ and γ are constitutive parameters.

The first problem we address is that of crack initiation. We will consider fixed initial crack lengths $\hat{a}_t = \hat{a}_b = 1$ and define the ratio $\phi = \hat{\sigma}_c^t/\hat{\sigma}_c^b$. When $\phi > 1$, the critical stress required to advance the top crack is smaller than that required to advance the bottom crack, suggesting that mode is preferred for initiation. When $\phi < 1$, bottom crack advancement is preferred. Defining an acceptable tolerance, e, a parameter regime with $|\phi - 1| > e$ should be demanded in order to avoid sensitivity of crack initiation to material defects.

Let us start by computing ϕ across the range of dimensionless parameters; results are presented in Fig. 4. In each case, the other parameters are fixed, with values given in Table 1. The figures indicate that increasing parameters η, ψ and γ makes initiation of the crack at the top of the sample more favourable, whereas increasing κ encourages crack initiation at the bottom of the sample. We now turn to the physical interpretation of the model and the implications

Table 1
A table of fixed values of the dimensionless parameters applied to generate the plots in Fig. 4.

η	ψ	κ	γ	E_f^*	G_f^*	G_c^*
2	2	300	−180	1.6×10^6	6.5×10^5	8.5×10^5

of these results. The parameter ψ increases when the sample thickness H increases, implying that increasing the sample thickness makes top debonding more favourable. We expect this because the applied stress has less influence at the bottom of the sample when the thickness is large. Similarly, the parameter η controls the exponential decay of the applied stress through the sample. When η is large, the decay is very steep and the applied stress has little influence on the stress state at the base of the sample.

Considering the non-geometric parameters γ and κ, these parameters influence the initiation of fracture in an expected manner. The parameter κ represents the dimensionless axial residual stress. When a crack advances from the bottom of the sample, these residual stresses are relaxed. This is not the case when the crack advances from the top, suggesting that increasing κ makes bottom debonding more favourable, increasing ϕ. This is observed in Fig. 4(c). The parameter γ represents the effect of interfacial friction in the dimensionless problem. When $|\gamma|$ is large, the resistance to crack advancement due to friction is large. Although this is true for both top and bottom debonding, it has a bigger effect on crack advancement from the bottom. This is because the applied stress has little impact on the stress distribution at the bottom of the sample. The process is almost entirely controlled by residual stresses favouring bottom debonding, opposed by friction preventing bottom debonding. Increasing friction therefore increases the stress required for bottom debonding much more than it increases the stress in top debonding.

Another interesting observation on the variation of ϕ is the relationship with the results of finite element modelling [26,27]. The result of the finite element modelling is that the mismatch in elastic coefficients between the fibre and the matrix plays a much more important role than the radial elastic residual strain. This is reflected in Fig. 4(d), in which varying γ over several orders of magnitude induces a much smaller change than the other parameters, particularly κ. We can explore this link further by assuming that the residual stresses are induced by an isotropic thermal contraction. In this case, the axial and radial strains will be of the same order of magnitude. However, the axial residual stress is proportional to the elastic modulus of the fibre, whereas the radial residual stress caused by the matrix 'clamping' is proportional to the elastic modulus of the matrix. The ratio of κ to γ will therefore be approximately the ratio between elastic coefficients. This demonstrates consistency between the observations that in some works, the elastic mismatch determines the debonding mechanism [26,27], while in others the mechanism of debonding changes due to axial residual stress [22].
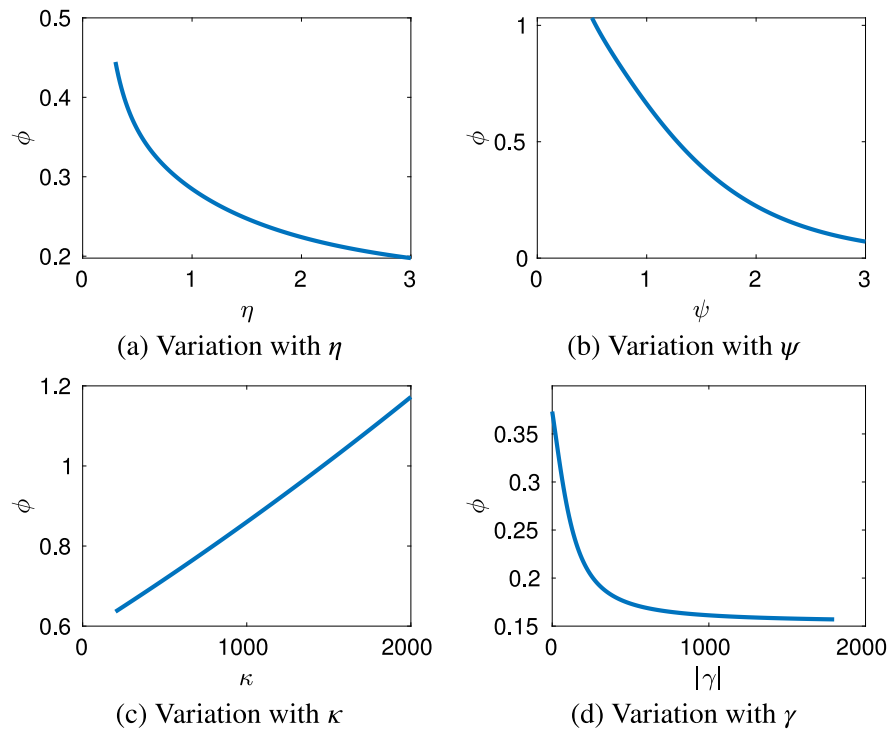
Fig. 4. Figures demonstrating the effect of the identified dimensionless parameters on the ratio of critical applied stresses in crack advancement ϕ.

Having determined the effect of the dimensionless parameters on crack initiation, we now aim to understand how the parameters affect the growth of cracks from the top and the bottom of the sample. In particular, let us focus on the stability of the crack advancement. Stability in crack advancement is important because when the crack is unstable, we cannot experimentally verify the mechanisms of debonding. We describe a crack as unstable when an infinitesimal increase in the absolute value of applied stress induces finite growth of the crack. Note that such an increase represents a decrease in the value of applied stress. One criteria for unstable growth, applied in the analysis of Fig. 5, is:

$$\frac{\mathrm{d}\hat{\sigma}^c}{\mathrm{d}\hat{a}} > 0. \tag{28}$$

A crack is described as stable if it is not unstable. In practice, it is experimentally desirable for the derivative to be less than zero. This ensures that the stability of the crack growth is unaffected by random defects in the interface. A formula for the derivative in terms of the critical stress and the quadratic parameters α, β and ω is given in Appendix B.

We will test the stability of with a predetermined intermediate length. Obviously, an intermediate length must be chosen with respect to the sample geometry. We will examine $\hat{a}_t = \hat{a}_b = \psi\eta$, half the dimensionless sample thickness. The effect of the dimensionless parameters on the stability of the advancing cracks is demonstrated in Fig. 5.

The geometric parameters influence the stability of the advancing crack with trends which are consistent with our physical understanding of the process. Increasing the parameter ψ encourages stability of the crack advancing from the top of the sample, conversely inhibiting the stability of the bottom crack. Larger sample thicknesses, controlled by ϕ, ensure that the top crack undergoes stable propagation because the elastic energy stored in the fibre in front of the crack tip is very small, implying that more work must be done on the system to advance the crack. For the bottom crack, the stress present in the fibre must already be very large, suggesting that when the crack advances, much more elastic energy is available in the fibre for fracture. Increasing η acts to stabilise both modes of cracking because the observed steeper decay of axial stress ensures that the work done by the loading system is the

main source of energy for fracture of either type to occur in the central area of the sample.

The parameters κ and γ also affect the stability of the advancing cracks in a predictable way. We see that κ acts to promote stability for both the top and bottom crack, having a larger effect on the crack advancement from the bottom of the sample. This is expected because larger residual stresses make crack initiation easier without affecting the elastic energy stored in the central regions of the fibre, implying that little energy is available for the crack to advance in these regions and that more work must be done on the system in order for either crack to propagate. Considering γ, we observe that increasing γ promotes stability for the top crack while inhibiting stability for the bottom crack. This is because increasing γ increases the stress required for bottom crack initiation, without affecting the fibre elastic stresses. Since the stress required for initiation is much larger, the elastic energy available from the fibre during crack advancement is much larger, promoting unstable advance.

Having deduced the effect of the different parametric contributions to the interfacial fracture process in using a general analysis based on dimensionless quantities, we now apply the model to validate the assumptions of previous analytic models for the fibre push-out test. We will analyse ceramic matrix composites and metal matrix composites.

3.2. Ceramic matrix composites

Classical push-out experiments indicate that in ceramic matrix composites, debonding initiates and undergoes stable propagation from the top of the sample [16], until the crack tip is approximately $3R_f/2$ away from the base of the sample. At this point, the influence of defects at the base of the sample induces an unstable advance of a crack from the base of the sample to complete the push-out.

However, recent in-situ testing on half fibres appears to indicate that a crack can initiate and undergo stable propagation from the base of the sample in SiC/BN/SiC composites [11]. Full fibre push-out tests performed in the same work indicate that the crack initiates from the top of the sample, suggesting substantial variability in mechanisms for
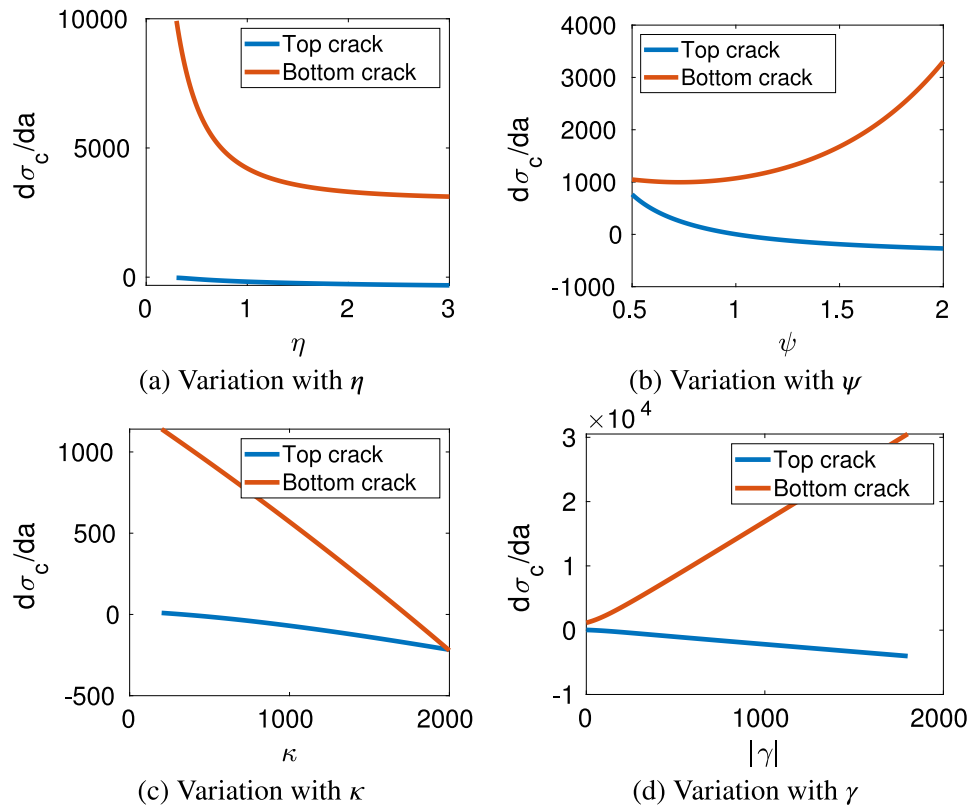
Fig. 5. Figures demonstrating the effect of the dimensionless parameters on the stability of the advancing cracks.

Table 2
A table of the constitutive parameters in each part of the CMC system.

	E(GPa)	ν
SiC_f	270 [29,30]	0.2 [30]
SiC_m	460 [31]	0.2 [32]
BN	20	0.22

Table 3
A table of the geometric parameters for the fibre push-out test of the SiC/BN/SiC composite. The thickness of the sample varies between 30 μm and 80 μm.

R_f	h	R_0
7 μm	0.2 μm	1000 μm

different thin samples. We will take the example of the SiC/BN/SiC composite and apply the model to it.

Constitutive information for the silicon carbide fibres and matrix and the boron nitride interface material is provided in Table 2. We will begin by considering a thick sample, for which experiments indicate the debonding process initiates from the top. The geometric information is summarised in Table 3. Due to the similarity of thermo-elastic properties between the fibre and the matrix, the elastic residual stresses within the system remain small [28]. Note that the residual stresses arising due to solidification of the system after CVI melt infiltration are not relieved by fibre push-out, implying that only the small thermal residual stresses are relaxed. We will assume a typical boundary residual stress of 50 MPa. Following the analysis of Callaway, the interfacial fracture energy measured is 1.2 N m⁻¹. The interfacial sliding stress, obtained by matching the width of hysteresis loops, is 30.3 MPa.

The key result of applying the model to the thick fibre push-out test is demonstrated in Fig. 6(a). For short crack lengths (less than 20 μm) the critical stress required for crack advancement from the top

is approximately eight times smaller than that required to advance a crack at the bottom of the sample of similar length. In this case, it is clear that the crack therefore initiates and develops from the top of the sample. Moreover, the critical stress required for debonding from the top is an increasing function of the crack length, implying that the crack growth is stable in this sample. This is in agreement with the available experimental data for thick sample testing [16].

Figs. 6(b)–6(d) demonstrate the evolution of the critical applied stresses in the sample when the thickness of the sample is varied. Decreasing the sample thickness does not affect the crack advancement profile for a crack propagating at the top of the sample to a great extent. In contrast, the sample thickness strongly influences the critical stress required for crack propagation at the bottom of the sample. For the thinnest sample, $H = 40$ μm, the stresses differ by a factor of approximately three for the shortest cracks. However, we still expect the crack to initiate and advance from the top of the sample. This suggests that when the crack propagates from the bottom, as observed in [11], some other parameter is influencing the balance between the top and bottom stresses.

The parametric study indicates that, within the model framework, the only possible parameter responsible is the residual stress. This is confirmed in Fig. 7. Fig. 7(a) indicates that even a substantial increase in residual stress is insufficient to change the crack initiation from the top to the bottom of the sample. However, the initiation stress for a crack from the bottom is comparable to the critical stress required for greater crack lengths propagating from the top. This implies that the interaction of advancing crack tips could be problematic for such systems.

In Fig. 7(b), the critical stress required for crack advancement from the bottom is less than for crack advancement from the top for short crack lengths, implying that when the sample has strong residual stresses, an interfacial crack advances from the bottom of the sample. However, after a short period of stable crack advancement from the bottom, a stable crack initiates from the top of the sample. The
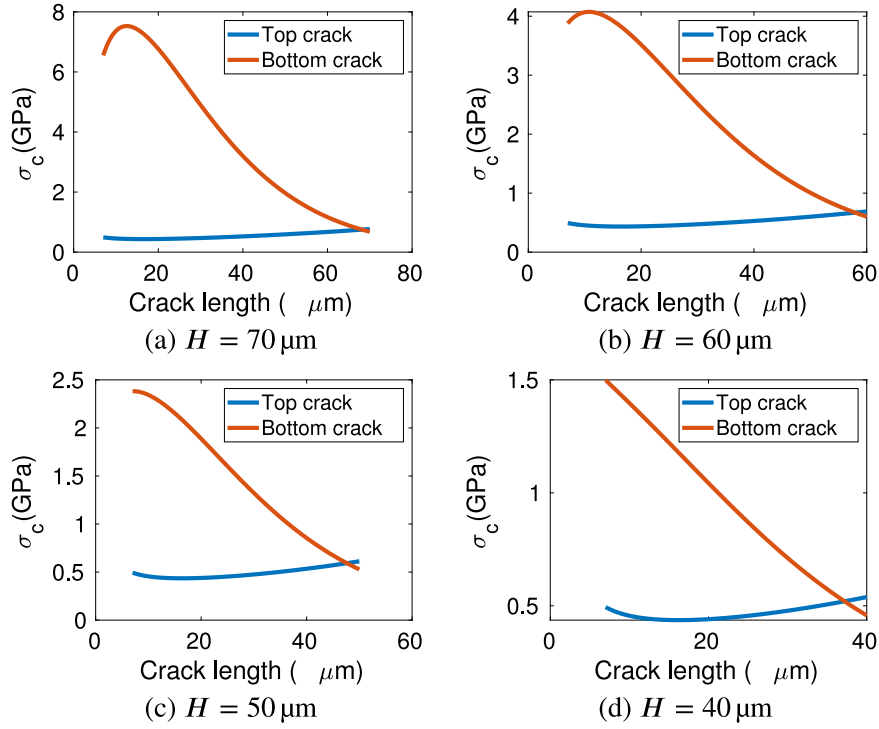
Fig. 6. Figures demonstrating how sample thickness affects the critical applied stress required for top and bottom crack advancement in CMC push-out testing. For each thickness, the critical applied stress is expressed as a function of the relevant crack length.
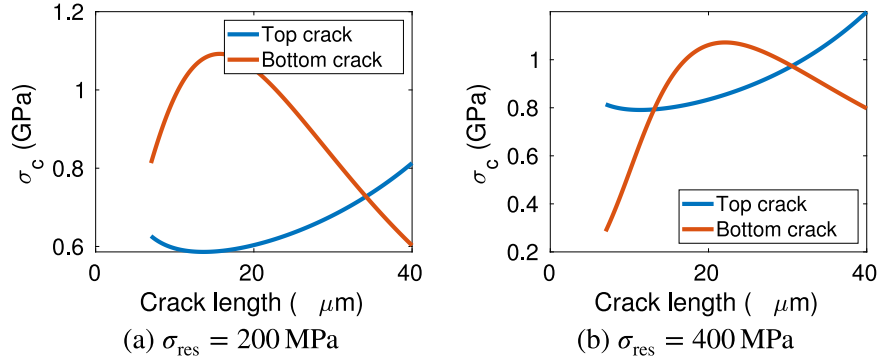

Fig. 7. Figures illustrating the transition from stable crack advancement from the top of the sample to unstable crack advancement from the bottom. The transition is caused by increasing the axial residual stress acting on the fibre.

current model and previous models do not cover the case of interacting cracks, suggesting that this combination of residual stresses and sample geometry should be avoided for CMCs.

Finally, we will use the case of a thick sample CMC problem to validate the model quantitatively. The sample is considered thick relative to the samples prepared for in-situ testing [11], with the ratio of sample thickness to fibre diameter exceeding 10. Fig. 8 demonstrates the application of the model to the 200 μm thick samples studied in the work of Gavalda-Diaz et al. [16]. The residual stresses are calibrated from the drop in load and constant sliding stress after complete debonding observed in the experimental literature. The load–displacement behaviour is computed by first obtaining the crack length as a function of the critical applied stress. The applied load is then varied from 0 to 400 mN. With each increment in the load, the applied stress is found and compared to the critical applied stress of the crack length at that increment. If the applied stress is greater than the critical stress, the crack length is increased until the critical stress exceeds the applied stress. The elastic displacement of the fibre is then computed from the

axial stress distribution by:

$$
\begin{aligned}
u_f &= \int_{-H/2}^{H/2} \frac{\sigma_f(z)}{E_f}\, \mathrm{d}z \\
&= \frac{1}{E_f}\left(\int_{H/2-L}^{H/2} \frac{2\bar{\tau}}{R_f}\left(z - \frac{H}{2}\right) + \sigma + \sigma_{\mathrm{res}}\, \mathrm{d}z \right. \\
&\quad \left. + \int_{-H/2}^{H/2-L} \frac{\sigma \cosh\left(\frac{z}{\eta R_f}\right)}{2\cosh\left(\frac{H}{2\eta R_f}\right)} + \frac{(\sigma + 2\sigma_{\mathrm{res}})\sinh\left(\frac{z}{\eta R_f}\right)}{2\sinh\left(\frac{H}{2\eta R_f}\right)}\, \mathrm{d}z \right).
\end{aligned}
\tag{29}
$$

The model performs very well for the experimental data points of Gavaldà-Diaz et al. [16]. Compared to the model of Callaway et al. [18], the predictions are similar, with slight corrections to that model arising due to the consideration of the sample thickness and the weak axial residual stresses. Overall, for thick sample CMC push-out tests, the new model performs better than the model of Callaway. However, the Callaway model gives a very similar prediction to the
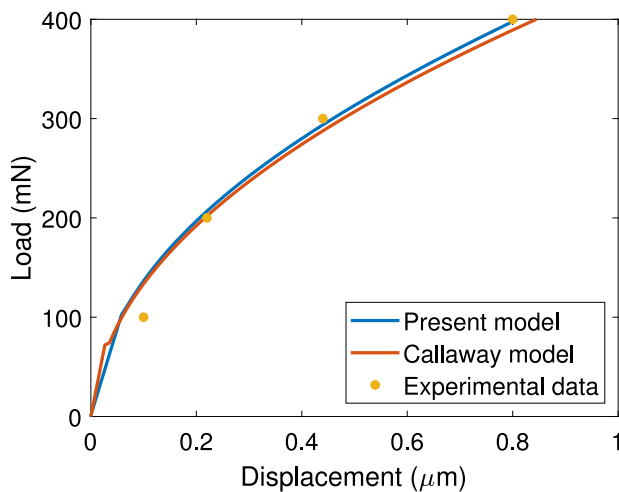
Fig. 8. Figure illustrating the predicted load–displacement behaviour of the thick sample fibre-push-out tests performed by Gavaldà-Diaz et al. plotted in comparison to the observed data values [16]. The model predictions are similar to those of the work of Callaway et al. [18], calibrated in the work of [16], also plotted.

Table 4
A table of the constitutive information in the metal matrix composite. The Young modulus of Timetal 834 is taken to be average [21].

	E (GPa)	ν
SCS-6	469	0.17
Timetal 834	90	0.3

present model, suggesting that neglecting axial residual stresses and the effect of sample thickness is appropriate for these experiments.

In summary, the model predicts that in most realistic cases, the crack develops and advances at the top of the sample. This agrees with the wealth of experimental data from classical push-out tests and with previous models for the fibre push-out test for CMCs. Moreover, the model demonstrates that strong residual stresses can cause the crack to propagate from the bottom of the sample. We will now further explore the link between axial residual stress and the micromechanics of fracture by examining fibre push-out tests of metal matrix composites.

3.3. Metal matrix composites

We now turn our attention to MMCs, with a particular focus on the Ti-SiC system studied by Sun [22]. One of the main differences between the CMC system and the MMC system is that the mismatch in thermo-elastic properties induces much stronger residual stresses when the test is performed at room temperature. Finite element modelling indicates that this is also the case for PMCs [33]. However, the thickness of the samples used in fibre push-out tests for MMCs is typically much larger than for CMCs, typically ranging from 200 μm to 600 μm [34]. Such geometry is typically chosen because the fibres in MMCs have a much larger radius than the fibres in CMCs. The study of CMCs demonstrated that thicker samples promote crack formation from the top of the sample, whereas strong residual stresses promote crack formation at the bottom of the sample, suggesting that the choice of geometry for MMC push-out tests is more complex.

In order to validate the model in this case, we will compare the computed values of fracture energy to those computed by the Sun model [22] and the value obtained by finite element simulation [21]. We take the interfacial sliding stress to be 717.3 MPa and the axial residual stress to be 839 MPa, with an applied load of 45 N and a crack length of 20 μm [22]. The thickness of the sample is 400 μm and the fibre radius is 71 μm. The resulting fracture energy from our model is

Table 5
A table of the geometric parameters for the fibre push-out test of the SCS-6/Timetal 834 composite. The thickness of the sample varies between 200 μm and 500 μm.

R_f	h	R_0
71 μm	0	1000 μm

47.7 J/m^2, comparable to the 45.6 J/m^2 computed by the Sun model and the 40 J/m^2 obtained by finite element analysis [21]. This demonstrates the applicability of the model to metal matrix fibre push-out tests.

We will now analyse the micromechanics of the debonding in the SCS-6/Timetal 834 composite across a range of sample thicknesses. Geometric and constitutive information for the analysis is provided in Tables 4 and 5. The result of applying the model across a range of thickness values is provided in Fig. 9. For samples thinner than 400 μm, the crack initiates and propagates from the bottom of the sample. This is in agreement with the assumption of previous works on MMCs [22,23]. Moreover, the critical applied stress is an increasing function of the crack length, implying that the crack development is stable. This is consistent with the parametric study, in which strong residual stresses acted to make bottom crack advancement stable.

In the case of a sample of thickness greater than 400 μm, indicated in Figs. 9(c) and 9(d), the micromechanical events involved in the debonding process are not clear. Initially, the model predicts that an interfacial crack will advance from the base of the sample. However, the critical applied stress required for advancement of the bottom crack at length of 120 μm is greater than that required to advance a very short crack from the top of the sample. Therefore, a crack may initiate and propagate from the top of the sample. In this case, we will have an interaction between the two advancing cracks, a case beyond the scope of this model. However, it is clear that the fracture process in this case is experimentally undesirable. We conclude that demanding predictable, stable crack advancement constrains the sample geometry in MMC push-out tests to a greater extent than previously assumed. For the SCS-6/Timetal 834 system, a maximum thickness of around 300 μm is suggested.

An important example of why it is important to consider the micromechanics of the debonding arises in the study of an SCS-6/Timetal 21 s system. The Sun model predicts a fracture energy of 38.9 J/m^2, whereas experimental analysis gives a value in the range 50-70 J/m^2 [35]. Taking the axial residual stress 736 MPa and the interfacial sliding stress 379.7 MPa, with a sample thickness of 540 μm, Fig. 10(a) demonstrates the crack propagation behaviour of the sample, assuming a fracture energy of 60 J/m^2. We see that in the course of the push out experiment, cracks will potentially advance from both the top and bottom of the sample. This leads to the underestimate of the Sun model because smaller stresses are required to achieve the same total crack length when both cracks advance. If it is assumed that the crack advances from only one face, the smaller critical stress for crack advancement leads to an underestimate of the ability of the material to resist fracture.

Fig. 10(b) demonstrates how choosing a thinner sample could avoid the problem of simultaneously advancing cracks, giving a test geometry more appropriate for existing characterisation techniques.

4. Conclusion

In conclusion, a new model for the fibre push-out test was formulated, taking into account the finite thickness of test samples and the effect of residual stresses in the fibre. The model was applied to the push-out test performed on a ceramic matrix composite with a thin interfacial layer of boron nitride. In addition, the model was applied to a test on a metal matrix composite. The objective of this study was to characterise the micromechanical events involved in interfacial fracture, with particular focus on determining whether the interfacial crack initiates at the top or the bottom of the sample.

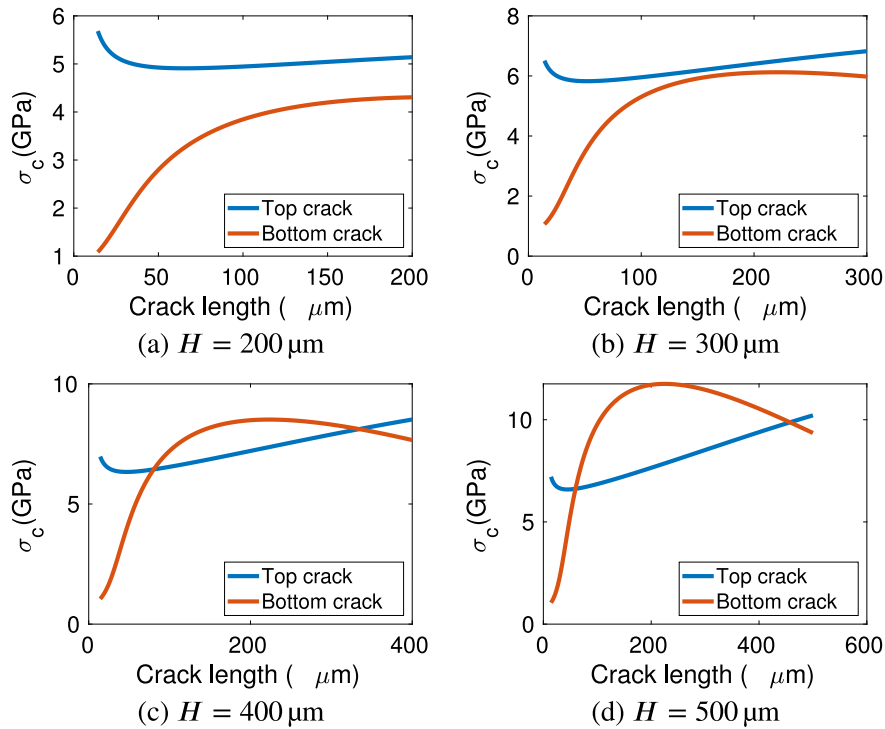The key conclusions of this work can be summarised as follows:

Fig. 9. Figures demonstrating the effect of sample thickness in the fibre push-out test for a metal matrix composite.
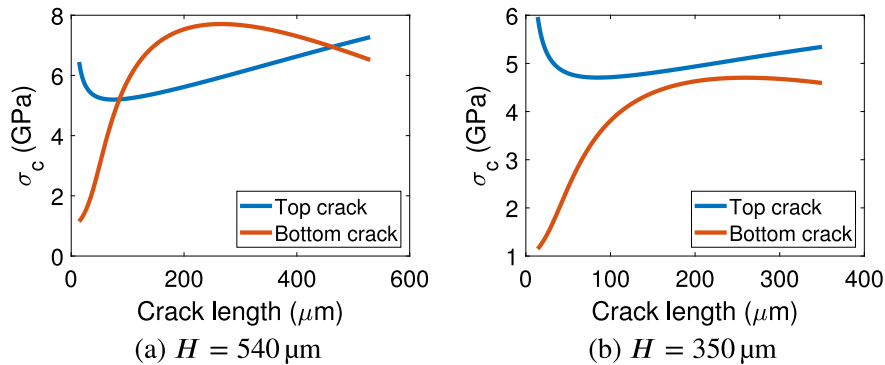

Fig. 10. Figures demonstrating the interaction between crack advancement mechanisms in an SCS-6/Timetal 21 s system. When the sample thickness is reduced to $350\,\mu$m, the crack solely advances from the bottom of the sample.

- Provided with the sample geometry and an estimate of the interfacial fracture energy, the new model accurately predicts the micromechanical events involved in interfacial fracture for both CMCs and MMCs. We conclude from this that the assumptions of previous models for the push-out test on those materials were well founded.
- The validity of the new model can be tested for a given sample geometry and material system by applying the quadratic coefficient criterion. Moreover, it was found that model validity can be assured independently of the interfacial properties, making the model suitable for new material systems in which residual stresses and interfacial friction are unknown.
- For new material systems, applying the model can determine the values of sample thickness for which the crack advancement is stable and the interaction between crack tips is minimal. In general, the model concludes that thinner samples are preferable for systems with strong residual stresses, while thick samples are advantageous for systems with weak residual stresses.

The model has successfully characterised the micromechanical events involved in the fibre push-out test. However, problems remain. One of

the assumptions made in formulating the model was that the interfacial sliding stress was constant across both crack areas. In general, the sliding stress on the top crack area is greater. Both the Poisson expansion of the fibre and the bending response of the matrix in thin samples apply radial compressive stresses to the top part of the interface, introducing stronger frictional resistance to debonding and sliding when the crack propagates from the top of the sample. Additionally, the present model considers only a mode-II fracture. For soft matrix materials like most PMCs, the bending response of the matrix induces tensile radial stresses at the bottom of the sample, suggesting that a mixed mode-I/mode-II crack opening is possible.

For future work, resolving the above difficulties is a priority. Additionally, one aspect of the model of Callaway [18] we have not incorporated is the yielding of the interfacial layer. Such yielding can influence the value of fracture energy computed experimentally and potentially influences the micromechanical events involved in the interfacial failure. Moreover, the model presented in this paper does not account for composites with a soft matrix material such as polymer matrix composites. Extending the model to the case of PMCs by accounting for the elastic deformation of the matrix and the energy

dispersed due to plasticity would represent a major generalisation to the model presented in this work.

CRediT authorship contribution statement

Benjamin Collard: Methodology, Software, Investigation, Formal analysis, Visualization, Writing – original draft. **Finn Giuliani:** Conceptualization, Resources, Supervision, Writing – review & editing. **Gerwin Ingenbleek:** Supervision, Writing – review & editing. **Guy Verbist:** Writing – review & editing. **Daniele Dini:** Conceptualization, Formal analysis, Supervision, Writing – original draft, Writing – review & editing, Resources.

Declaration of competing interest

The authors declare the following financial interests/personal relationships which may be considered as potential competing interests: Benjamin Collard reports financial support was provided by Shell Global Solutions international BV.

Acknowledgements

Appendix A. Contributions to energy

This appendix contains explicit derivations for each of the contributions to the energy release rate. We begin with the contribution due to end shortening. By definition, $E_{\text{end}} = \sigma \pi R_f^2 \delta$. Applying the fundamental theorem of calculus, we deduce:

$$
\begin{aligned}
\frac{d E_{\text{end}}}{d a_b} &= \pi \sigma R_f^2 \frac{d \delta}{d a_b} \\
&= \frac{\pi \sigma R_f^2}{E_f} \left(\frac{2\bar{\tau}}{R_f} a_b - \left(\frac{\sigma \cosh\left(\frac{a_b}{\eta R_f} - \psi \right)}{2 \cosh(\psi)} \right.\right. \\
&\quad \left.\left. + \frac{(\sigma + 2\sigma_{\text{res}}) \sinh\left(\frac{a_b}{\eta R_f} - \psi \right)}{2 \sinh(\psi)} \right) \right).
\end{aligned}
\tag{30}
$$

Similarly:

$$
\begin{aligned}
\frac{d E_{\text{end}}}{d a_t} &= \frac{\pi \sigma R_f^2}{E_f} \left(\sigma + \sigma_{\text{res}} - \frac{2\bar{\tau}}{R_f} a_t - \left(\frac{\sigma \cosh\left(\psi - \frac{a_t}{\eta R_f} \right)}{2 \cosh(\psi)} \right.\right. \\
&\quad \left.\left. + \frac{(\sigma + 2\sigma_{\text{res}}) \sinh\left(\psi - \frac{a_t}{\eta R_f} \right)}{2 \sinh(\psi)} \right) \right).
\end{aligned}
\tag{31}
$$

For the elastic coating, the total energy stored is:

$$
\begin{aligned}
E_{\text{elast, coat}} &= \frac{\pi \left((h + R_f)^2 - R_f^2 \right)}{2 G_c} \int_{-H/2}^{H/2} \tau(z)^2 \, dz \\
&= \frac{\pi \left((h + R_f)^2 - R_f^2 \right)}{2 G_c} \left(\int_{-H/2}^{a_b - H/2} \bar{\tau}^2 \, dz + \int_{a_b - H/2}^{H/2 - a_t} \tau_f(z)^2 \, dz \right. \\
&\quad \left. + \int_{H/2 - a_t}^{H/2} \bar{\tau}^2 \, dz \right).
\end{aligned}
\tag{32}
$$

We again apply the fundamental theorem of calculus:

$$
\begin{aligned}
\frac{d E_{\text{elast, coat}}}{d a_b} &= \frac{\pi \left((h + R_f)^2 - R_f^2 \right)}{2 G_c} \left(\bar{\tau}^2 - \frac{1}{4\eta^2} \left(\frac{\sigma \sinh\left(\frac{a_b}{\eta R_f} - \psi \right)}{2 \cosh(\psi)} \right.\right. \\
&\quad \left.\left. + \frac{(\sigma + 2\sigma_{\text{res}}) \cosh\left(\frac{a_b}{\eta R_f} - \psi \right)}{2 \sinh(\psi)} \right)^2 \right) \\[6pt]
\frac{d E_{\text{elast, coat}}}{d a_t} &= \frac{\pi \left((h + R_f)^2 - R_f^2 \right)}{2 G_c} \left(\bar{\tau}^2 - \frac{1}{4\eta^2} \left(\frac{\sigma \sinh\left(\psi - \frac{a_t}{\eta R_f} \right)}{2 \cosh(\psi)} \right.\right. \\
&\quad \left.\left. + \frac{(\sigma + 2\sigma_{\text{res}}) \cosh\left(\psi - \frac{a_t}{\eta R_f} \right)}{2 \sinh(\psi)} \right)^2 \right).
\end{aligned}
\tag{33}
$$

The energy stored in the fibre due to shear deformation is similarly derived as:

$$
\begin{aligned}
\frac{d E_{\text{elast, shear}}}{d a_b} &= \frac{\pi R_f^2}{2 G_f} \left(\bar{\tau}^2 - \frac{1}{4\eta^2} \left(\frac{\sigma \sinh\left(\frac{a_b}{\eta R_f} - \psi \right)}{2 \cosh(\psi)} \right.\right. \\
&\quad \left.\left. + \frac{(\sigma + 2\sigma_{\text{res}}) \cosh\left(\frac{a_b}{\eta R_f} - \psi \right)}{2 \sinh(\psi)} \right)^2 \right) \\[6pt]
\frac{d E_{\text{elast, shear}}}{d a_t} &= \frac{\pi R_f^2}{2 G_f} \left(\bar{\tau}^2 - \frac{1}{4\eta^2} \left(\frac{\sigma \sinh\left(\psi - \frac{a_t}{\eta R_f} \right)}{2 \cosh(\psi)} \right.\right. \\
&\quad \left.\left. + \frac{(\sigma + 2\sigma_{\text{res}}) \cosh\left(\psi - \frac{a_t}{\eta R_f} \right)}{2 \sinh(\psi)} \right)^2 \right).
\end{aligned}
\tag{34}
$$

Finally, the energy stored in the fibre by the axial deformation is

$$
E_{\text{elast, axial}} = \frac{\pi R_f^2}{2 E_f} \int_{-H/2}^{H/2} \sigma_f(z)^2 \, dz.
\tag{35}
$$

Applying the fundamental theorem of calculus:

$$
\begin{aligned}
\frac{d E_{\text{elast, axial}}}{d a_b} &= \frac{\pi R_f^2}{2 E_f} \left(\left(\frac{2\bar{\tau}}{R_f} a_b \right)^2 - \left(\frac{\sigma \cosh\left(\frac{a_b}{\eta R_f} - \psi \right)}{2 \cosh(\psi)} \right.\right. \\
&\quad \left.\left. + \frac{(\sigma + 2\sigma_{\text{res}}) \sinh\left(\frac{a_b}{\eta R_f} - \psi \right)}{2 \sinh(\psi)} \right)^2 \right) \\[6pt]
\frac{d E_{\text{elast, axial}}}{d a_t} &= \frac{\pi R_f^2}{2 E_f} \left(\left(\sigma + \sigma_{\text{res}} - \frac{2\bar{\tau}}{R_f} a_t \right)^2 - \left(\frac{\sigma \cosh\left(\psi - \frac{a_t}{\eta R_f} \right)}{2 \cosh(\psi)} \right.\right. \\
&\quad \left.\left. + \frac{(\sigma + 2\sigma_{\text{res}}) \sinh\left(\psi - \frac{a_t}{\eta R_f} \right)}{2 \sinh(\psi)} \right)^2 \right).
\end{aligned}
\tag{36}
$$

We must finally consider the work done by the system against friction. Given an inelastic slide $w_s(z)$ on the top crack area, the work done against $\bar{\tau}$ is given by [22]:

$$E_{\text{fric}} = 2\pi R_f \int_{H/2-a_t}^{H/2} |\bar{\tau} \parallel w_s(z)| \, \mathrm{d}z. \tag{37}$$

Computing $w_s(z)$:

$$
\begin{aligned}
w_s(z) &= \frac{1}{E_f} \int_{H/2-a_t}^{z} \frac{\sigma \cosh\left(\frac{\bar{z}}{\eta R_f}\right)}{2\cosh(\psi)} + \frac{(\sigma+2\sigma_{\text{res}})\sinh\left(\frac{\bar{z}}{\eta R_f}\right)}{2\sinh(\psi)} \\
&\quad - \left(\frac{2\bar{\tau}}{R_f}\left(\bar{z}-\frac{H}{2}\right) + \sigma + \sigma_{\text{res}}\right) \mathrm{d}\bar{z} \\
&= \frac{\eta R_f \sigma}{2E_f \cosh(\psi)}\left(\sinh\left(\frac{\bar{z}}{\eta R_f}\right) - \sinh\left(\psi - \frac{a_t}{\eta R_f}\right)\right) \\
&\quad + \frac{\eta R_f(\sigma+2\sigma_{\text{res}})}{2E_f \sinh(\psi)}\left(\cosh\left(\frac{\bar{z}}{\eta R_f}\right) - \cosh\left(\psi - \frac{a_t}{\eta R_f}\right)\right) \\
&\quad - \frac{\bar{\tau}}{E_f R_f}\left(\left(z-\frac{H}{2}\right)^2 - a_t^2\right) - \frac{\sigma+\sigma_{\text{res}}}{E_f}\left(z + a_t - \frac{H}{2}\right).
\end{aligned}
\tag{38}
$$

Note that we can apply the Leibniz integral rule in Eq. (37). We have:

$$
\begin{aligned}
\frac{\mathrm{d}E_{\text{fric}}}{\mathrm{d}a_t} &= 2\pi R_f |\bar{\tau}| \frac{\mathrm{d}}{\mathrm{d}a_t}\int_{H/2-a_t}^{H/2} w_s(z)\,\mathrm{d}z \\
&= 2\pi R_f |\bar{\tau}|\left(w_s\left(\frac{H}{2}-a_t\right) + \int_{H/2-a_t}^{H/2}\frac{\mathrm{d}}{\mathrm{d}a_t}w_s(z)\,\mathrm{d}z\right) \\
&= \frac{2\pi R_f |\bar{\tau}|a_t}{E_f}\left(\frac{\sigma\cosh\left(\psi-\frac{a_t}{\eta R_f}\right)}{2\cosh(\psi)} + \frac{(\sigma+2\sigma_{\text{res}})\sinh\left(\psi-\frac{a_t}{\eta R_f}\right)}{2\sinh(\psi)}\right. \\
&\quad \left. + \frac{2\bar{\tau}a_t}{R_f} - (\sigma+\sigma_{\text{res}})\right)
\end{aligned}
\tag{39}
$$

An analogous line of reasoning applies to the work done against friction for the bottom crack. For the bottom crack, we have:

$$\frac{\mathrm{d}E_{\text{fric}}}{\mathrm{d}a_b} = 2\pi R_f |\bar{\tau}|\left(w_s\left(a_b - \frac{H}{2}\right) + \int_{-H/2}^{a_b-H/2}\frac{\mathrm{d}}{\mathrm{d}a_b}w_s(z)\,\mathrm{d}z\right) \tag{40}$$

By continuity of displacement, we have $w_s(z) = 0$ at the crack tip. Moreover, by definition, we have:

$$
\begin{aligned}
w_s(z) &= \frac{1}{E_f}\int_{z}^{a_b-H/2}\frac{\sigma\cosh\left(\frac{\bar{z}}{\eta R_f}\right)}{2\cosh(\psi)} + \frac{(\sigma+2\sigma_{\text{res}})\sinh\left(\frac{\bar{z}}{\eta R_f}\right)}{2\sinh(\psi)} \\
&\quad - \frac{2\bar{\tau}}{R_f}\left(\bar{z}+\frac{H}{2}\right)\mathrm{d}\bar{z}.
\end{aligned}
\tag{41}
$$

By the fundamental theorem of calculus:

$$
\begin{aligned}
\frac{\mathrm{d}}{\mathrm{d}a_b}w_s(z) &= \frac{1}{E_f}\left(\frac{\sigma\cosh\left(\frac{a_b}{\eta R_f}-\psi\right)}{2\cosh(\psi)} + \frac{(\sigma+2\sigma_{\text{res}})\sinh\left(\frac{a_b}{\eta R_f}-\psi\right)}{2\sinh(\psi)}\right. \\
&\quad \left. - \frac{2\bar{\tau}a_b}{R_f}\right).
\end{aligned}
\tag{42}
$$

We can therefore conclude that:

$$
\begin{aligned}
\frac{\mathrm{d}E_{\text{fric}}}{\mathrm{d}a_b} &= \frac{2\pi R_f |\bar{\tau}|a_b}{E_f}\left(\frac{\sigma\cosh\left(\frac{a_b}{\eta R_f}-\psi\right)}{2\cosh(\psi)} + \frac{(\sigma+2\sigma_{\text{res}})\sinh\left(\frac{a_b}{\eta R_f}-\psi\right)}{2\sinh(\psi)}\right. \\
&\quad \left. - \frac{2\bar{\tau}a_b}{R_f}\right).
\end{aligned}
\tag{43}
$$

Appendix B. Critical stress formulae

In computing the fracture energy, we arrived at a quadratic relationship between the critical stress for crack advancement and the fracture energy. We expressed this relationship in the form:

$$\Gamma = \alpha\sigma_c^2 + \beta\sigma_c + \omega. \tag{44}$$

We may apply the quadratic formula to this equation in order to derive formulae for the critical stresses:

$$\sigma_c = \frac{-\beta \pm \sqrt{\beta^2 - 4\alpha(\omega - \Gamma)}}{2\alpha}. \tag{45}$$

Two problems arise in this formula. Firstly, it is not immediately clear which root we should choose. However, for a compressive push-out test, we expect σ_c to be negative. Since $\alpha > 0$ is the test for model validity, we therefore select the most negative solution, taking the negative square root. Secondly, it is not true that for any choice of the parameters the value of σ_c is real. However, one simple criteria for real solutions is $\omega - \Gamma < 0$, which is trivially satisfied when $\omega < 0$. This is the case for the examples examined in this work.

To compute the derivative, observe that Eq. (44) implies that:

$$
\begin{aligned}
0 &= \frac{\mathrm{d}}{\mathrm{d}a}\left(\alpha\sigma_c^2 + \beta\sigma_c + \omega\right) \\
&= \frac{\mathrm{d}\alpha}{\mathrm{d}a}\sigma_c^2 + \frac{\mathrm{d}\beta}{\mathrm{d}a}\sigma_c + \frac{\mathrm{d}\omega}{\mathrm{d}a} + 2a\sigma_c\frac{\mathrm{d}\sigma_c}{\mathrm{d}a} + \beta\frac{\mathrm{d}\sigma_c}{\mathrm{d}a}.
\end{aligned}
\tag{46}
$$

Rearranging, the derivative of the critical stress with respect to the crack length is:

$$\frac{\mathrm{d}\sigma_c}{\mathrm{d}a} = -\frac{\frac{\mathrm{d}\alpha}{\mathrm{d}a}\sigma_c^2 + \frac{\mathrm{d}\beta}{\mathrm{d}a}\sigma_c + \frac{\mathrm{d}\omega}{\mathrm{d}a}}{2a\sigma_c + \beta}. \tag{47}$$

References

[1] Roger R. Naslain, The design of the fibre-matrix interfacial zone in ceramic matrix composites, Composites A (ISSN: 1359-835X) 29 (9) (1998) 1145–1155, http://dx.doi.org/10.1016/S1359-835X(97)00128-0, URL https://www.sciencedirect.com/science/article/pii/S1359835X97001280.

[2] He Ming-Yuan, John W. Hutchinson, Crack deflection at an interface between dissimilar elastic materials, Int. J. Solids Struct. (ISSN: 0020-7683) 25 (9) (1989) 1053–1067, http://dx.doi.org/10.1016/0020-7683(89)90021-8, URL https://www.sciencedirect.com/science/article/pii/0020768389900218.

[3] F.W. Zok, Ceramic-matrix composites enable revolutionary gains in turbine engine efficiency, Am. Ceramic Soc. Bull. (ISSN: 0002-7812) 95 (5) (2016) 22–28.

[4] Roger R. Naslain, SiC-Matrix composites: Nonbrittle ceramics for thermostructural application, Int. J. Appl. Ceram. Technol. 2 (2) (2005) 75–84, http://dx.doi.org/10.1111/j.1744-7402.2005.02009.x, URL https://ceramics.onlinelibrary.wiley.com/doi/abs/10.1111/j.1744-7402.2005.02009.x.

[5] B. Yu, T.J. Katafiasz, S. Nguyen, G. Allegri, J. Finlayson, E.S. Greenhalgh, S.T. Pinho, S. Pimenta, Hygrothermal effects on the translaminar fracture toughness of a highly toughened aerospace CFRP: Experimental characterisation and model prediction, Composites A (ISSN: 1359-835X) 150 (2021) 106582, http://dx.doi.org/10.1016/j.compositesa.2021.106582, URL https://www.sciencedirect.com/science/article/pii/S1359835X2100302X.

[6] A.G. Evans, F.W. Zok, The physics and mechanics of fibre-reinforced brittle matrix composites, J. Mater. Sci. (ISSN: 1573-4803) 29 (15) (1994) 3857–3896, http://dx.doi.org/10.1007/BF00355946.

[7] Roger R. Naslain, René J.-F. Pailler, Jacques L. Lamon, Single- and multilayered interphases in SiC/SiC composites exposed to severe environmental conditions: An overview, Int. J. Appl. Ceram. Technol. 7 (3) (2010) 263–275, http://dx.doi.org/10.1111/j.1744-7402.2009.02424.x, URL https://ceramics.onlinelibrary.wiley.com/doi/abs/10.1111/j.1744-7402.2009.02424.x.

[8] Xiaoyu Cao, Xiaowei Yin, Xiaomeng Fan, Laifei Cheng, Litong Zhang, Effect of PyC interphase thickness on mechanical behaviors of sibc matrix modified c/SiC composites fabricated by reactive melt infiltration, Carbon (ISSN: 0008-6223) 77 (2014) 886–895, http://dx.doi.org/10.1016/j.carbon.2014.05.092, URL https://www.sciencedirect.com/science/article/pii/S000862231400548X.

[9] G. Catalanotti, A.R. Melro, R.P. Tavares, B.G. Falzon, L.F. Varandas, Micromechanical modelling of the longitudinal compressive and tensile failure of unidirectional composites: The effect of fibre misalignment introduced via a stochastic process, Int. J. Solids Struct. (ISSN: 0020-7683) 203 (2020) 157–176, http://dx.doi.org/10.1016/j.ijsolstr.2020.07.022, https://www.sciencedirect.com/science/article/pii/S0020768320302997.

[10] William A. Curtin, Theory of mechanical properties of ceramic-matrix composites, J. Am. Ceram. Soc. 74 (11) (1991) 2837–2845, http://dx.doi.org/10.1111/j.1151-2916.1991.tb06852.x, URL https://ceramics.onlinelibrary.wiley.com/doi/abs/10.1111/j.1151-2916.1991.tb06852.x.

[11] Robin M.G. De Meyere, Kay Song, Louise Gale, Stephen Harris, Ian M. Edmonds, Thomas J. Marrow, Eduardo Saiz, Finn Giuliani, David E.J. Armstrong, Oriol Gavaldà-Diaz, A novel trench fibre push-out method to evaluate interfacial failure in long fibre composites, J. Mater. Res. (ISSN: 2044-5326) (2021) http://dx.doi.org/10.1557/s43578-021-00153-1.

[12] Andreas J. Brunner, Fracture mechanics testing of fiber-reinforced polymer composites: The effects of the "human factor" on repeatability and reproducibility of test data, Eng. Fract. Mech. (ISSN: 0013-7944) 264 (2022) 108340, http://dx.doi.org/10.1016/j.engfracmech.2022.108340, URL https://www.sciencedirect.com/science/article/pii/S0013794422000996.

[13] Ronald J. Kerans, Triplicane A. Parthasarathy, Theoretical analysis of the fiber pullout and pushout tests, J. Am. Ceram. Soc. 74 (7) (1991) 1585–1596, http://dx.doi.org/10.1111/j.1151-2916.1991.tb07144.x, URL https://ceramics.onlinelibrary.wiley.com/doi/abs/10.1111/j.1151-2916.1991.tb07144.x.

[14] A.F. Kalton, S.J. Howard, J. Janczak-Rusch, T.W. Clyne, Measurement of interfacial fracture energy by single fibre push-out testing and its application to the titanium–silicon carbide system, Acta Mater. (ISSN: 1359-6454) 46 (9) (1998) 3175–3189, http://dx.doi.org/10.1016/S1359-6454(98)00009-3, URL https://www.sciencedirect.com/science/article/pii/S1359645498000093.

[15] C. Liang, J.W. Hutchinson, Mechanics of the fiber pushout test, Mech. Mater. (ISSN: 0167-6636) 14 (3) (1993) 207–221, http://dx.doi.org/10.1016/0167-6636(93)90067-2, URL https://www.sciencedirect.com/science/article/pii/0167663693900672.

[16] Oriol Gavalda-Diaz, Riccardo Manno, Antonio Melro, Giuliano Allegri, Stephen R. Hallett, Luc Vandeperre, Eduardo Saiz, Finn Giuliani, Mode I and mode II interfacial fracture energy of SiC/BN/SiC CMCs, Acta Mater. (ISSN: 1359-6454) 215 (2021) 117125, http://dx.doi.org/10.1016/j.actamat.2021.117125, URL https://www.sciencedirect.com/science/article/pii/S135964542100505X.

[17] C.H. Hsueh, F. Rebillat, J. Lamon, E. Lara-Curzio, Analyses of fiber push-out tests performed on Nicalon/SiC composites with tailored interfaces, Compos. Eng. (ISSN: 0961-9526) 5 (10) (1995) 1387–1401, http://dx.doi.org/10.1016/0961-9526(95)99801-A, URL https://www.sciencedirect.com/science/article/pii/096195269599801A.

[18] E.B. Callaway, P.G. Christodoulou, F.W. Zok, Deformation, rupture and sliding of fiber coatings in ceramic composites, J. Mech. Phys. Solids (ISSN: 0022-5096) 132 (2019) 103673, http://dx.doi.org/10.1016/j.jmps.2019.07.016, URL https://www.sciencedirect.com/science/article/pii/S0022509619304193.

[19] Yu Gong, Junan Tao, Xinjian Chen, Jian Zhao, Ning Hu, A semi-analytical method for determining mode-II fracture toughness and bridging law of composite laminates, Eng. Fract. Mech. (ISSN: 0013-7944) 265 (2022) 108371, http://dx.doi.org/10.1016/j.engfracmech.2022.108371, URL https://www.sciencedirect.com/science/article/pii/S001379442200128X.

[20] V.T Bechel, N.R Sottos, A comparison of calculated and measured debond lengths from fiber push-out tests, Compos. Sci. Technol. (ISSN: 0266-3538) 58 (11) (1998) 1727–1739, http://dx.doi.org/10.1016/S0266-3538(98)00038-4, URL https://www.sciencedirect.com/science/article/pii/S0266353898000384.

[21] W.D Zeng, P.W.M Peters, Y. Tanaka, Interfacial bond strength and fracture energy at room and elevated temperature in titanium matrix composites (SCS-6/Timetal 834), Composites A (ISSN: 1359-835X) 33 (9) (2002) 1159–1170, http://dx.doi.org/10.1016/S1359-835X(02)00089-1, URL https://www.sciencedirect.com/science/article/pii/S1359835X02000891.

[22] Q. Sun, X. Luo, Y.Q. Yang, Z.H. Xia, R.J. Zhang, J.H. Lou, C.L. Xue, Evaluation on the interfacial fracture toughness of fiber-reinforced titanium matrix composites by push out test, Compos. Interfaces 23 (7) (2016) 557–569, http://dx.doi.org/10.1080/09276440.2016.1156916.

[23] M.N. Yuan, Y.Q. Yang, Z.H. Xia, Modeling of push-out test for interfacial fracture toughness of fiber-reinforced composites, Adv. Compos. Mater. 21 (5–6) (2012) 401–412, http://dx.doi.org/10.1080/09243046.2012.738631.

[24] M.P. Thomas, M.R. Winstone, Longitudinal yielding behaviour of SiC-fibre-reinforced titanium-matrix composites, Compos. Sci. Technol. (ISSN: 0266-3538) 59 (2) (1999) 297–303, http://dx.doi.org/10.1016/S0266-3538(98)00072-4, URL https://www.sciencedirect.com/science/article/pii/S0266353898000724.

[25] Peng Xu, Renshu Yang, Yang Guo, Cheng Chen, Yang Yang, Jinjing Zuo, Investigation of the interaction mechanism of two dynamic propagating cracks under blast loading, Eng. Fract. Mech. (ISSN: 0013-7944) 259 (2022) 108112, http://dx.doi.org/10.1016/j.engfracmech.2021.108112, URL https://www.sciencedirect.com/science/article/pii/S0013794421005208.

[26] G. Lin, P.H. Geubelle, N.R. Sottos, Simulation of fiber debonding with friction in a model composite pushout test, Int. J. Solids Struct. (ISSN: 0020-7683) 38 (46) (2001) 8547–8562, http://dx.doi.org/10.1016/S0020-7683(01)00085-3, URL https://www.sciencedirect.com/science/article/pii/S0020768301000853.

[27] V.T. Bechel, N.R. Sottos, Application of debond length measurements to examine the mechanics of fiber pushout, J. Mech. Phys. Solids (ISSN: 0022-5096) 46 (9) (1998) 1675–1697, http://dx.doi.org/10.1016/S0022-5096(97)00040-9, URL https://www.sciencedirect.com/science/article/pii/S0022509697000409.

[28] Kaitlin Kollins, Craig Przybyla, Maher S. Amer, Residual stress measurements in melt infiltrated SiC/SiC ceramic matrix composites using Raman spectroscopy, J. Euro. Ceram. Soc. (ISSN: 0955-2219) 38 (7) (2018) 2784–2791, http://dx.doi.org/10.1016/j.jeurceramsoc.2018.02.013, URL https://www.sciencedirect.com/science/article/pii/S0955221918300876.

[29] Jacques Lamon, Stéphane Mazerat, Mohamed R'Mili, Reinforcement of ceramic matrix composites: Properties of SiC-based filaments and tows, in: Ceramic Matrix Composites, John Wiley & Sons, Ltd, ISBN: 9781118832998, 2014, pp. 1–26, http://dx.doi.org/10.1002/9781118832998.ch1, Chapter 1, URL https://onlinelibrary.wiley.com/doi/abs/10.1002/9781118832998.ch1.

[30] Ö. Ünal, Narottam P. Bansal, In-plane and interlaminar shear strength of a unidirectional hi-nicalon fiber-reinforced celsian matrix composite, Ceram. Int. (ISSN: 0272-8842) 28 (5) (2002) 527–540, http://dx.doi.org/10.1016/S0272-8842(02)00006-8, URL https://www.sciencedirect.com/science/article/pii/S0272884202000068.

[31] Yevhen Zayachuk, Phani Karamched, Christian Deck, Peter Hosemann, David E.J. Armstrong, Linking microstructure and local mechanical properties in SiC-SiC fiber composite using micromechanical testing, Acta Mater. (ISSN: 1359-6454) 168 (2019) 178–189, http://dx.doi.org/10.1016/j.actamat.2019.02.001, URL https://www.sciencedirect.com/science/article/pii/S1359645419300783.

[32] J.-L. Bobet, J. Lamon, Thermal residual stresses in ceramic matrix composites— I. Axisymmetrical model and finite element analysis, Acta Metall. Et Mater. (ISSN: 0956-7151) 43 (6) (1995) 2241–2253, http://dx.doi.org/10.1016/0956-7151(94)00429-3, URL https://www.sciencedirect.com/science/article/pii/0956715194004293.

[33] Jun Wang, Yajie Feng, Gang Zhao, Lingwei Yang, Jian Xu, Effect of elastic and thermal mismatch on push-in mechanism and shear strength measurement of fiber/matrix interface, Compos. Interfaces 27 (10) (2020) 921–935, http://dx.doi.org/10.1080/09276440.2020.1712917.

[34] Yingwei Fan, Xiaorong Zhou, Investigation of interface debonding behaviour in a unidirectional SiC fibre reinforced Ti-17 composite by a single fibre push-out technique, J. Compos. Mater. (2021) 1–9, http://dx.doi.org/10.1177/00219983211031653.

[35] S. Mukherjee, C.R. Ananth, N. Chandra, Effects of interface chemistry on the fracture properties of titanium matrix composites, Composites A (ISSN: 1359-835X) 29 (9) (1998) 1213–1219, http://dx.doi.org/10.1016/S1359-835X(97)00129-2, URL https://www.sciencedirect.com/science/article/pii/S1359835X97001292.